Efficient Interlayer Exciton Transport in Two-Dimensional Metal-Halide Perovskites.

Alvaro J. Magdaleno,[1,2] Michael Seitz,[1,2] Michel Frising,[1,2] Ana Herranz de la Cruz,[1,2] Antonio I. Fernández-Domínguez,[1,3] and Ferry Prins[1,2]*

1. Condensed Matter Physics Center (IFIMAC), Universidad Autónoma de Madrid, 28049 Madrid, Spain.

2. Departamento de Física de la Materia Condensada, Universidad Autónoma de Madrid, 28049 Madrid, Spain.

3. Departamento de Física Teórica de la Materia Condensada, Universidad Autónoma de Madrid, 28049 Madrid, Spain

AUTHOR INFORMATION

Corresponding Author

* Email: ferry.prins@uam.es

Abstract

Two-dimensional (2D) metal-halide perovskites are attractive for use in light harvesting and light emitting devices, presenting improved stability as compared to the more conventional three-dimensional perovskite phases. Significant attention has been given to influence of the layer orientation of 2D perovskites phases, with charge-carrier transport through the plane of the material being orders of magnitude more efficient than interlayer transport. Importantly though, the thinnest members of the 2D perovskite family exhibit strong exciton binding energies, suggesting that interlayer energy transport mediated by dipole-dipole coupling may be relevant. We present transient microscopy measurements of interlayer energy transport in $(PEA)_2PbI_4$ perovskite. We find efficient interlayer exciton transport (0.06 cm^2/s), which translates into a diffusion length that exceeds 100 nm and a sub-ps timescale for energy transfer. While still slower than in-plane exciton transport (0.2 cm^2/s), our results show that excitonic energy transport is considerably less anisotropic than charge-carrier transport for 2D perovskites.

Layered metal-halide perovskites have emerged as a more robust analogue to their three-dimensional counterparts, displaying better moisture and air resistance.[1,2] Their structure is composed of corner-sharing metal-halide octahedra described by the general formula $L_2[ABX_3]_{n-1}BX_4$, where A is a small cation (e.g. methylammonium, formamidinium), B is a divalent metal cation (e.g. lead, tin), X is a halide anion (chloride, bromide, iodide), L is a long organic cation, and n is the number of octahedra that make up the thickness of the inorganic layer. The improved stability comes from the passivating role of the long organic cations that separate the inorganic structure into layers.[3,4] Recent reports have shown that solar cells[5–8] and light emitting diodes[9–14] based on 2D perovskites can combine high performance with prolonged stability.

To efficiently incorporate 2D perovskites in optoelectronic technologies, the layer orientation becomes an important parameter for device performance. Specifically, charge transport through the inorganic layer is much more efficient than transport between different layers, which requires tunneling of charges across the barrier imposed by the insulating long organic cations.[15] Indeed, several studies have highlighted the importance of layer orientation to promote charge transport between the electrodes and improve device performance.[16–23]

However, when the 2D perovskites reach small layer thicknesses ($n \leq 5$), quantum and dielectric confinement effects become relevant and charge carriers form bound electron-hole pairs known as excitons.[24,25] Like charge carriers, excitons can move readily through the crystalline plane of the perovskite.[26–28] However, while interlayer transfer of charge carriers is inefficient, excitons can potentially transfer efficiently from one layer to another through dipole-dipole coupling.[29–31] Dipole-dipole coupling in layered perovskites is expected to be particularly strong as these materials exhibit large oscillator strengths (> 10 Debye) and favorable dipole alignment.[32]

To date, energy transfer studies in 2D perovskites have been focused exclusively on films of mixed dimensionality, studying the transfer between phases of distinct layer thickness (i.e. phases of different n) using time resolved spectroscopy.[13,33] This downhill energy transfer process is of particular relevance in hybrid 2D-3D perovskite solar cells, where phases of distinct n co-exist.[15] The transfer between perovskite layers of identical thickness, however, has not been studied yet. As a result of the small Stokes shifts (< 100 meV)[34,35] a significant spectral overlap exists between the emission and absorption of layers of identical thickness. This suggests not only that efficient energy transfer between layers of identical thickness is possible, but moreover that sequential energy-transfer may lead to transport of excitons across significant length-scales in the out-of-plane (OP) direction within a phase of identical layer thickness.

Here, we use transient photoluminescence microscopy to directly visualize the OP exciton transport in single crystals of $n = 1$ phenethylammonium lead iodine perovskites $((PEA)_2PbI_4)$.[26,31,36] By performing these measurements on different facets of the crystal, we can directly compare the OP with the in-plane (IP) exciton transport characteristics of this material. We find a significant OP diffusivity (0.06 cm^2/s) and diffusion length (>100 nm), which is only moderately less than the IP characteristics (~ 0.2 cm^2/s and 200 nm). Consequently, the exciton transport in this material is much less anisotropic than charge carrier transport, for which several orders of magnitude difference between IP and OP has been reported.[15] Importantly, the observed high interlayer diffusivity translates to energy transfer between individual layers on a sub-ps timescale. Using numerical simulations, we show that such ultrafast timescales are over two orders of magnitude faster than predictions using Förster theory. We discuss the shortcomings of Förster theory for the specific case of excitons in layered perovskites and the implications of efficient interlayer exciton transport for device design.
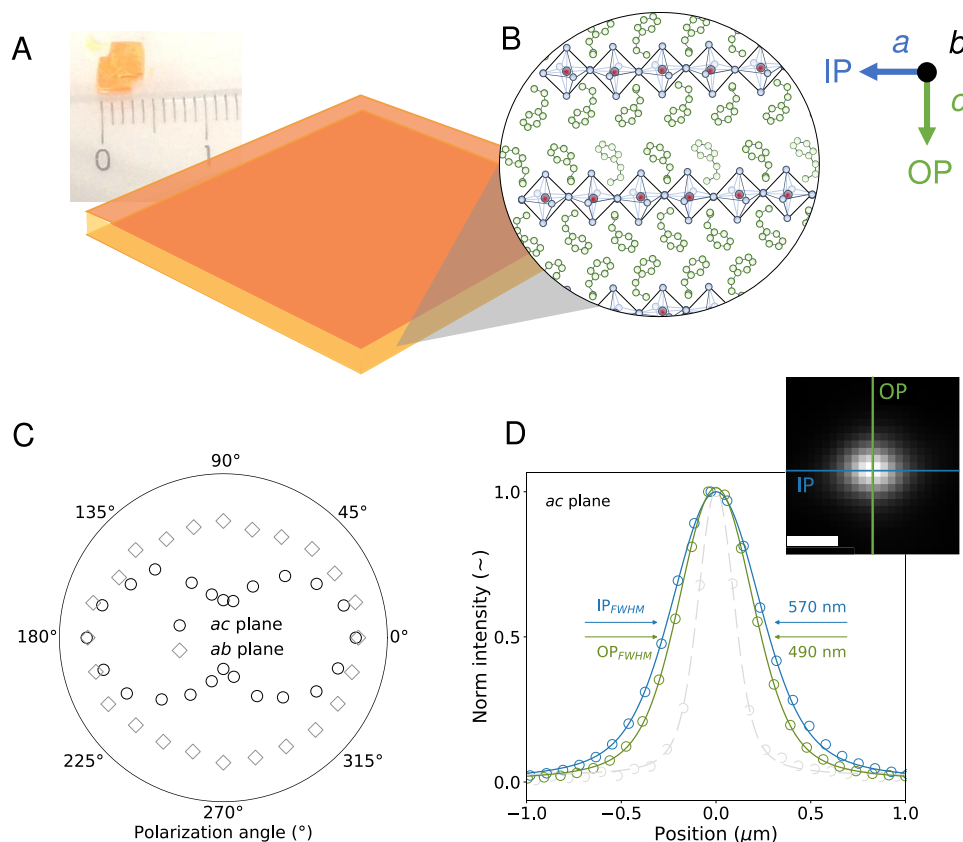
Figure 1. (A) Crystal structure of the (PEA)$_2$PbI$_4$ layered perovskite along the b axis, illustrating the inorganic PbI$_4$ layers (red and blue) separated by organic PEA cations (green). (B) Millimeter-sized single crystal obtained using slow-growth from a saturated precursor solution. (C) Photoluminescence intensity as a function of polarization for the *ab* crystal plane (blue diamonds) and *ac* crystal plane (green circles) of a single crystal of (PEA)$_2$PbI$_4$. The polarization orientation is aligned with the crystallographic a-axis at 0° (D) Emission profile along the IP (blue) and OP (green) axes from a near-diffraction limited excitation spot on the *ac* crystal plane of a (PEA)$_2$PbI$_4$ crystal (inset with scale bar of 500 nm). Dashed grey line shows the directly imaged laser excitation profile.

We grow millimeter-sized single crystals of $(PEA)_2PbI_4$ by slow crystallization from a saturated precursor solution (see **Figure 1A** and Supporting information for more details). $(PEA)_2PbI_4$ is characterized by a strong excitonic absorption peak (λ_{abs} = 2.42 eV) and a narrow photoluminescent emission spectrum (λ_{em} = 2.37 eV), resulting in a modest Stokes shift (ΔE_{Stokes} = 50 meV, see **Figure S1**). The crystal structure of $(PEA)_2PbI_4$ is shown along the *b*-axis in **Figure 1B**, illustrating its layered nature of organic PEA cations separating the inorganic octahedra of the PbI_4 layer with a center-to-center separation *d* of 1.64 nm between the inorganic layers.[37] The anisotropic environment yields an exciton that is confined to a 2D plane, which is reflected in the polarization of the photoluminescence from the different crystal planes. While emission from the *ab* crystal plane is isotropic, strongly polarized emission is observed from the *ac* crystal plane[38], as is shown in **Figure 1C**. The strong polarization is consistent with a strong IP orientation of the transition dipole of the excitons.[39–41]

To gain qualitative insight in the exciton transport along the IP and OP directions of the crystal, we look at the photoluminescence emission profile following near-diffraction-limited excitation (λ_{ex} = 405 nm, FWHM = 250 nm). While the excitation profile is fully symmetric, we observe a distinctly asymmetric emission profile on the *ac* crystal plane that is elongated along the IP direction (see **Figure 1D**). This is in contrast to the symmetric emission profile that is obtained on the *ab* crystal plane (see **Figure S3**), which is consistent with earlier reports of isotropic IP exciton transport in $(PEA)_2PbI_4$.[26–28] The asymmetry on the *ac* plane suggests IP energy transport is more efficient than OP transport. Crucially though, the OP emission profile is still considerably wider than the excitation profile, suggesting exciton transport through interlayer energy transfer to be significant.
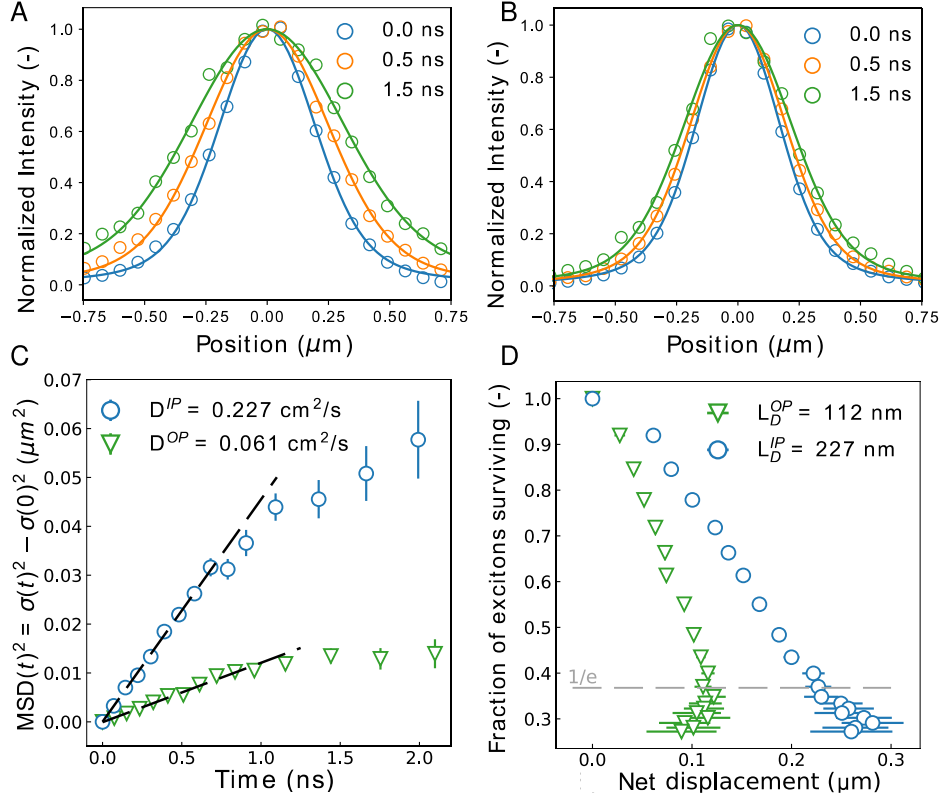
Figure 2. (A), (B) IP and OP emission profiles for different times after excitation. Solid lines are fits to a Voigt function. (C) Time-evolution of the mean-square-displacement $(\text{MSD}(t) = \sigma(t)^2 - \sigma(0)^2$, which is the change in variance of the Voigt profiles) of the exciton population along both the IP (blue) and OP (green) direction. (D) Fractions of surviving excitons as a function of net spatial displacement $\sqrt{MSD(t)}$ of excitons for IP (green) and OP (blue) direction. Reported errors represent the uncertainty in the fitting procedure.

To quantify the exciton transport characteristics along the different axes, we use transient photoluminescence microscopy (TPLM). In short, we place a scanning avalanche photodiode (20 μm in size) in the magnified (330 x) image plane of the emission profile. Using pulsed laser excitation (< 200 ps), fluorescence lifetime traces are recorded for different positions along the

emission profile, allowing for a reconstruction of the time evolution of the exciton population with sub-nanosecond precision.[26,31,36] The results of the exciton transport measurements for the IP and OP axes are shown in **Figure 2A** and **B**, respectively. The emission profile along the IP axis shows a rapid broadening in the first nanosecond after excitation. In contrast, the broadening along the OP axis is significantly slower, though still clearly resolvable.

The widths of the exciton population can be quantified by fitting each time-slice with a Voigt function and extracting the variance, $\sigma(t)^2$. In **Figure 2C**, we plot the time-evolution of the mean-square-displacement (MSD) of the exciton population along both the IP and OP axes, given by $\text{MSD}(t) = \sigma(t)^2 - \sigma(0)^2$. To extract the diffusivity (D) of the excitons, we fit the early time dynamics (t < 0.75 ns) where normal diffusion is observed, with the one-dimensional diffusion equation, $\text{MSD}(t) = 2Dt$. The obtained IP diffusivity of $D_{IP} = 0.227 \pm 0.045$ cm^2/s is consistent with earlier measurements of the IP exciton transport in $(PEA)_2PbI_4$ prepared with the same method.[26] The diffusivity for OP transport is over a factor three smaller, measuring $D_{OP} = 0.061 \pm 0.026$ cm^2/s. Along both the IP and OP axes, the initial linear broadening is followed by a regime of slower diffusion, indicative of trap-state limited transport.[26]

To quantify the diffusion length, we check how far excitons traveled up to the moment in which only 1/e of excitons are left (see **Figure 2D**). We extract the number of excitons surviving from a multiexponential fit of the PL decay of **Figure S2**.[26] The difference in diffusivity along the two axes results in a reduction in the diffusion length from 227 ± 13 nm for the IP transport to 112 ± 20 nm for the OP transport. While this difference is notable, it shows that OP transport through interlayer energy transfer occurs across length scales that are significant for device operation.[42]

The OP diffusivity can be translated to an interlayer energy transfer rate k_{ET} assuming a one-dimensional random walk model.[42] Using the Smoluchowski-Einstein relation we obtain an interlayer energy transfer rate of $k_{ET} = 2D / d^2 = 4.5 \pm 1.9$ ps^{-1}, meaning an exciton hops to the next layer on average every 220 fs. This sub-picosecond timescale agrees with transfer rates reported for excitonic energy transfer between perovskite phases of different layer thicknesses.[33]
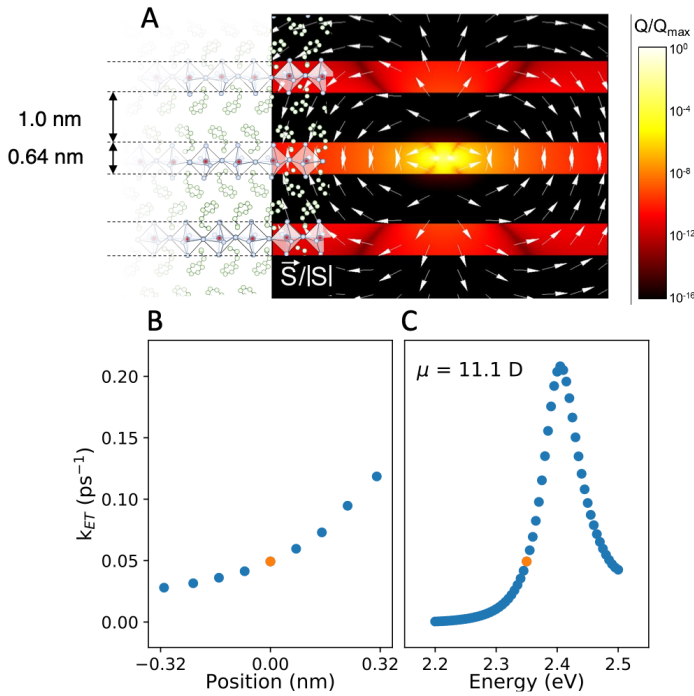

Figure 3. (A) Normalized absorption power density profile generated by the exciton dipole-like source present in the inorganic layer. Arrows describe the direction of the Poynting vector along the perovskite structure. Simulation obtained from numerical solutions of Maxwell's Equations. (B) Numerical energy transfer rate k_{ET} as a function of the vertical position of the donor dipole within the inorganic layer. (C) Dependence of the energy transfer rate on the donor emission frequency. Orange circle correspond to the originally calculated energy transfer rate (vertical position = 0 nm, donor emission frequency ~2.35 eV, $\mu = 11.1$ D).

We can compare the experimentally obtained interlayer energy transfer rate with predictions for the Förster dipole-dipole interactions describing through numerical solutions of Maxwell's Equations using COMSOL Multiphysics. To do so, we numerically evaluate the electric field and Poynting vector due to an in-plane oriented exciton dipole-like source, as well as the power absorbed in the neighboring layers. These simulations were parameterized with known literature values for the layer thicknesses[37] and the intrinsic anisotropic dielectric function of the organic and inorganic layers (see **Figure S4**).[43] The contourplot in **Figure 3A** shows the normalized absorbed power density, whose spatial profile follows the electric field intensity. We can observe that most of the absorption takes place in the layer where the exciton is located. The white arrows render the normalized Poynting vector, illustrating the confinement effect of the electromagnetic fields in the vicinity of the dipole source. The energy transfer can be computed by integrating the absorbed power density within the volume, V, of the first (upper or lower) neighboring inorganic layer as:

$$k_{ET} = \frac{2}{\hbar} \int_V \, d\boldsymbol{r} \, \text{Im}\{\boldsymbol{E}^*(\boldsymbol{r}, \omega_e)\boldsymbol{D}(\boldsymbol{r}, \omega_e)\} \tag{1}$$

where $\boldsymbol{E}(\boldsymbol{r}, \omega_e)$ and $\boldsymbol{D}(\boldsymbol{r}, \omega_e) = \epsilon_0\epsilon(\boldsymbol{r}, \omega_e)\boldsymbol{E}(\boldsymbol{r}, \omega_e)$ are the electric and displacement fields due to the excitonic source, evaluated at the emission frequency ω_e. Note that the moduli of both fields scale with the exciton dipole strength, μ, and $k_{ET} \propto \mu^2$. For (PEA)$_2$PbI$_4$ an IP dipole strength of 11.1 D was recently reported,[32] yielding an energy transfer rate of $k_{ET} = 0.05$ ps^{-1}. This rate is substantially slower than the experimental observation ($k_{ET} = 4.5$ ps^{-1}). While some uncertainty may be present in the reported value of the dipole strength, the quadratic scaling of the transfer

rate with the μ inherent to Eq. (1) would require exceedingly large values to reach sub-picosecond timescales.

The large discrepancy between experiment and simulation suggests significant short-comings of Förster theory in describing the dynamics of energy transfer in 2D perovskites. A fundamental assumption that underlies Förster theory is the point-dipole approximation. For semiconductor nanomaterials this approximation may not be strictly valid due to the relatively large spatial extend of the excitonic wavefunction. In particular, the extension of the exciton wavefunction in the OP direction could lead to a smaller effective dipole-dipole separation. To illustrate the potential influence of this, **Figure 3B** shows the energy transfer rate as a function of a vertical displacement of the donor dipole within the inorganic layer. As expected, bringing the dipole closer to the acceptor yields an enhanced rate. However, the effect is modest, reaching a factor 2.5 for maximum displacement of 0.32 nm with respect to the middle plane of the PbI_4 layer.

Finally, it is important to consider the consequence of the ultrafast timescale of energy transfer. Specifically, the ultrafast energy transfer rates are in direct competition with carrier relaxation to the band edge (260 fs),[44] suggesting that hot-exciton transfer processes may be relevant in determining the transfer rate. The influence of such non-equilibrium dynamics is expected to effectively shift the emission frequency towards the absorption band in the dielectric function of PbI_4.[45] To estimate this effect, we plot the energy transfer rate obtained from Eq. (1) as a function of the emission frequency in **Figure 3C**. We can observe that a four-fold enhancement is obtained at the absorption maximum. Our theory predicts that the spatial and spectral effects considered above could yield energy transfer rates in the 0.5 ps^{-1}, still one order of magnitude lower than the experimental one.

Let us remark that an additional consequence of the extended wavefunction is the possibility of quadrupolar interactions. Indeed, for energy transfer in semiconductor nanomaterials with relatively short donor-acceptor separations, it has been suggested that quadrupolar interactions may even exceed dipolar interactions.[46] Such interactions are not captured within our simple Förster model and may partially explain the underestimation of the transfer rate by Eq. (1).

In conclusion, we have demonstrated that interlayer energy transfer in $(PEA)_2PbI_4$ is highly efficient, resulting in significant energy transport along the OP direction of this material. Consequently, exciton transport in layered perovskites is considerably less anisotropic than charge carrier transport.[15] The layer orientation of the thinnest members of the 2D perovskite family may therefore be less important in device performance. In addition, our observation of sub-picosecond energy transfer has important implications for the fundamental dynamics of the optical excited state in 2D perovskites. Specifically, Auger recombination at high excitation densities will be highly suppressed due to the fast transfer to neighbouring layers, and may prove beneficial to light emitting devices.[47] Finally, we have shown that the origin of this ultrafast timescale lies beyond conventional Forster theory, and adds to similar observations of energy transfer in other 2D systems.[30,48] Further studies will be needed to elaborate the details of the underlying physics.

ASSOCIATED CONTENT

Supporting Information.

Detailed sample preparation, absorbance, photoluminescence, emission profile and exciton diffusion measurements and the determination of the intrinsic optical constants.

AUTHOR INFORMATION

Corresponding author

Ferry Prins, ferry.prins@uam.es

Author Contributions

A.J.M. prepared the samples and performed the measurements. A.J.M. and M.S. analyzed the transient microscopy measurements. A.I.F.D. performed theoretical modelling with assistance from A.J.M. and M.F. A.H. assisted in sample preparation. F.P. supervised the project. A.J.M. and F.P. wrote the manuscript. All authors contributed to the interpretation of the data and preparation of the manuscript.

REFERENCES

(1)   Yang, S.; Fu, W.; Zhang, Z.; Chen, H.; Li, C. Z. Recent Advances in Perovskite Solar Cells: Efficiency, Stability and Lead-Free Perovskite. *J. Mater. Chem. A* **2017**, *5* (23), 11462–11482.

(2)   Smith, I. C.; Hoke, E. T.; Solis-Ibarra, D.; McGehee, M. D.; Karunadasa, H. I. A Layered Hybrid Perovskite Solar-Cell Absorber with Enhanced Moisture Stability. *Angew. Chemie - Int. Ed.* **2014**, *53* (42), 11232–11235.

(3)   Fu, Q.; Tang, X.; Huang, B.; Hu, T.; Tan, L.; Chen, L.; Chen, Y. Recent Progress on the Long-Term Stability of Perovskite Solar Cells. *Adv. Sci.* **2018**, *5* (5), 1700387.

(4)   Quan, L. N.; Yuan, M.; Comin, R.; Voznyy, O.; Beauregard, E. M.; Hoogland, S.; Buin, A.; Kirmani, A. R.; Zhao, K.; Amassian, A.; Kim, D. H.; Sargent, E. H. Ligand-Stabilized Reduced-Dimensionality Perovskites. *J. Am. Chem. Soc.* **2016**, *138* (8), 2649–2655.

(5)   Liu, Y.; Akin, S.; Pan, L.; Uchida, R.; Arora, N.; Milić, J. V.; Hinderhofer, A.; Schreiber, F.; Uhl, A. R.; Zakeeruddin, S. M.; Hagfeldt, A.; Ibrahim Dar, M.; Grätzel, M. Ultrahydrophobic 3D/2D Fluoroarene Bilayer-Based Water-Resistant Perovskite Solar Cells with Efficiencies Exceeding 22%. *Sci. Adv.* **2019**, *5* (6), 1–9.

(6)   Grancini, G.; Roldán-Carmona, C.; Zimmermann, I.; Mosconi, E.; Lee, X.; Martineau, D.; Narbey, S.; Oswald, F.; De Angelis, F.; Graetzel, M.; Nazeeruddin, M. K. One-Year Stable Perovskite Solar Cells by 2D/3D Interface Engineering. *Nat. Commun.* **2017**, *8*, 1–8.

(7)   Yang, R.; Li, R.; Cao, Y.; Wei, Y.; Miao, Y.; Tan, W. L.; Jiao, X.; Chen, H.; Zhang, L.; Chen, Q.; Zhang, H.; Zou, W.; Wang, Y.; Yang, M.; Yi, C.; Wang, N.; Gao, F.; McNeill, C. R.; Qin, T.; Wang, J.; Huang, W. Oriented Quasi-2D Perovskites for High Performance Optoelectronic Devices. *Advanced Materials*. Advanced Materials 2018.

(8)   Ortiz-Cervantes, C.; Carmona-Monroy, P.; Solis-Ibarra, D. Two-Dimensional Halide Perovskites in Solar Cells: 2D or Not 2D? *ChemSusChem* **2019**, *12* (8), 1560–1575.

(9)   Veldhuis, S. A.; Boix, P. P.; Yantara, N.; Li, M.; Sum, T. C.; Mathews, N.; Mhaisalkar, S. G. Perovskite Materials for Light-Emitting Diodes and Lasers. *Adv. Mater.* **2016**, *28* (32), 6804–6834.

(10)   Zhang, L.; Liu, Y.; Yang, Z.; Liu, S. (Frank). Two Dimensional Metal Halide Perovskites:

Promising Candidates for Light-Emitting Diodes. *J. Energy Chem.* **2019**, *37*, 97–110.

(11) Xing, J.; Zhao, Y.; Askerka, M.; Quan, L. N.; Gong, X.; Zhao, W.; Zhao, J.; Tan, H.; Long, G.; Gao, L.; Yang, Z.; Voznyy, O.; Tang, J.; Lu, Z. H.; Xiong, Q.; Sargent, E. H. Color-Stable Highly Luminescent Sky-Blue Perovskite Light-Emitting Diodes. *Nat. Commun.* **2018**, *9* (1), 1–8.

(12) Tsai, H.; Nie, W.; Blancon, J. C.; Stoumpos, C. C.; Soe, C. M. M.; Yoo, J.; Crochet, J.; Tretiak, S.; Even, J.; Sadhanala, A.; Azzellino, G.; Brenes, R.; Ajayan, P. M.; Bulović, V.; Stranks, S. D.; Friend, R. H.; Kanatzidis, M. G.; Mohite, A. D. Stable Light-Emitting Diodes Using Phase-Pure Ruddlesden–Popper Layered Perovskites. *Adv. Mater.* **2018**, *30* (6), 1–9.

(13) Yuan, M.; Quan, L. N.; Comin, R.; Walters, G.; Sabatini, R.; Voznyy, O.; Hoogland, S.; Zhao, Y.; Beauregard, E. M.; Kanjanaboos, P.; Lu, Z.; Kim, D. H.; Sargent, E. H. Perovskite Energy Funnels for Efficient Light-Emitting Diodes. *Nat. Nanotechnol.* **2016**, *11* (10), 872–877.

(14) Congreve, D. N.; Weidman, M. C.; Seitz, M.; Paritmongkol, W.; Dahod, N. S.; Tisdale, W. A. Tunable Light-Emitting Diodes Utilizing Quantum-Confined Layered Perovskite Emitters. *ACS Photonics* **2017**, *4* (3), 476–481.

(15) Lin, Y.; Fang, Y.; Zhao, J.; Shao, Y.; Stuard, S. J.; Nahid, M. M.; Ade, H.; Wang, Q.; Shield, J. E.; Zhou, N.; Moran, A. M.; Huang, J. Unveiling the Operation Mechanism of Layered Perovskite Solar Cells. *Nat. Commun.* **2019**, *10* (1), 1–11.

(16) Chen, A. Z.; Shiu, M.; Ma, J. H.; Alpert, M. R.; Zhang, D.; Foley, B. J.; Smilgies, D. M.;

Lee, S. H.; Choi, J. J. Origin of Vertical Orientation in Two-Dimensional Metal Halide Perovskites and Its Effect on Photovoltaic Performance. *Nat. Commun.* **2018**, *9* (1), 1–7.

(17)   Abbas, M. S.; Hussain, S.; Zhang, J.; Wang, B.; Yang, C.; Wang, Z.; Wei, Z.; Ahmad, R. Orientationally Engineered 2D/3D Perovskite for High Efficiency Solar Cells. *Sustain. Energy Fuels* **2019**, *4* (1), 324–330.

(18)   Cao, D. H.; Stoumpos, C. C.; Farha, O. K.; Hupp, J. T.; Kanatzidis, M. G. 2D Homologous Perovskites as Light-Absorbing Materials for Solar Cell Applications. *J. Am. Chem. Soc.* **2015**, *137* (24), 7843–7850.

(19)   Tsai, H.; Nie, W.; Blancon, J. C.; Stoumpos, C. C.; Asadpour, R.; Harutyunyan, B.; Neukirch, A. J.; Verduzco, R.; Crochet, J. J.; Tretiak, S.; Pedesseau, L.; Even, J.; Alam, M. A.; Gupta, G.; Lou, J.; Ajayan, P. M.; Bedzyk, M. J.; Kanatzidis, M. G.; Mohite, A. D. High-Efficiency Two-Dimensional Ruddlesden-Popper Perovskite Solar Cells. *Nature* **2016**, *536* (7616), 312–317.

(20)   Soe, C. M. M.; Nie, W.; Stoumpos, C. C.; Tsai, H.; Blancon, J. C.; Liu, F.; Even, J.; Marks, T. J.; Mohite, A. D.; Kanatzidis, M. G. Understanding Film Formation Morphology and Orientation in High Member 2D Ruddlesden–Popper Perovskites for High-Efficiency Solar Cells. *Adv. Energy Mater.* **2018**, *8* (1), 2–11.

(21)   Liao, Y.; Liu, H.; Zhou, W.; Yang, D.; Shang, Y.; Shi, Z.; Li, B.; Jiang, X.; Zhang, L.; Quan, L. N.; Quintero-Bermudez, R.; Sutherland, B. R.; Mi, Q.; Sargent, E. H.; Ning, Z. Highly Oriented Low-Dimensional Tin Halide Perovskites with Enhanced Stability and Photovoltaic Performance. *J. Am. Chem. Soc.* **2017**, *139* (19), 6693–6699.

(22)   Chen, A. Z.; Choi, J. J. Crystallographic Orientation and Layer Impurities in Two-Dimensional Metal Halide Perovskite Thin Films. *J. Vac. Sci. Technol. A* **2020**, *38* (1), 010801.

(23)   Chen, A. Z.; Shiu, M.; Deng, X.; Mahmoud, M.; Zhang, D.; Foley, B. J.; Lee, S. H.; Giri, G.; Choi, J. J. Understanding the Formation of Vertical Orientation in Two-Dimensional Metal Halide Perovskite Thin Films. *Chem. Mater.* **2019**, *31* (4), 1336–1343.

(24)   Katan, C.; Mercier, N.; Even, J. Quantum and Dielectric Confinement Effects in Lower-Dimensional Hybrid Perovskite Semiconductors. *Chem. Rev.* **2019**, *119* (5), 3140–3192.

(25)   Gélvez-Rueda, M. C.; Hutter, E. M.; Cao, D. H.; Renaud, N.; Stoumpos, C. C.; Hupp, J. T.; Savenije, T. J.; Kanatzidis, M. G.; Grozema, F. C. Interconversion between Free Charges and Bound Excitons in 2D Hybrid Lead Halide Perovskites. *J. Phys. Chem. C* **2017**, *121* (47), 26566–26574.

(26)   Seitz, M.; Magdaleno, A. J.; Alcázar-Cano, N.; Meléndez, M.; Lubbers, T. J.; Walraven, S. W.; Pakdel, S.; Prada, E.; Delgado-Buscalioni, R.; Prins, F. Exciton Diffusion in Two-Dimensional Metal-Halide Perovskites. *Nat. Commun.* **2020**, *11* (1), 1–8.

(27)   Deng, S.; Shi, E.; Yuan, L.; Jin, L.; Dou, L.; Huang, L. Long-Range Exciton Transport and Slow Annihilation in Two-Dimensional Hybrid Perovskites. *Nat. Commun.* **2020**, *11* (1), 1–8.

(28)   Ziegler, J. D.; Zipfel, J.; Meisinger, B.; Menahem, M.; Zhu, X.; Taniguchi, T.; Watanabe, K.; Yaffe, O.; Egger, D. A.; Chernikov, A. Fast and Anomalous Exciton Diffusion in Two-Dimensional Hybrid Perovskites. Nano Lett. **2020**, 20, 6674−6681.

(29)   Zhang, Q.; Linardy, E.; Wang, X.; Eda, G. Excitonic Energy Transfer in Heterostructures of Quasi-2D Perovskite and Monolayer WS2. ACS Nano **2020**, 14, 11482−11489

(30)   Liu, J.; Guillemeney, L.; Abécassis, B.; Coolen, L. Long Range Energy Transfer in Self-Assembled Stacks of Semiconducting Nanoplatelets. *Nano Lett.* **2020**, *20* (5), 3465–3470.

(31)   Akselrod, G. M.; Prins, F.; Poulikakos, L. V.; Lee, E. M. Y.; Weidman, M. C.; Mork, A. J.; Willard, A. P.; Bulović, V.; Tisdale, W. A. Subdiffusive Exciton Transport in Quantum Dot Solids. *Nano Lett.* **2014**, *14* (6), 3556–3562.

(32)   Proppe, A. H.; Walters, G. W.; Alsalloum, A. Y.; Zhumekenov, A. A.; Mosconi, E.; Kelley, S. O.; De Angelis, F.; Adamska, L.; Umari, P.; Bakr, O. M.; Sargent, E. H. Transition Dipole Moments of n = 1, 2, and 3 Perovskite Quantum Wells from the Optical Stark Effect and Many-Body Perturbation Theory. *J. Phys. Chem. Lett.* **2020**, *11* (3), 716–723.

(33)   Proppe, A. H.; Elkins, M. H.; Voznyy, O.; Pensack, R. D.; Zapata, F.; Besteiro, L. V.; Quan, L. N.; Quintero-Bermudez, R.; Todorovic, P.; Kelley, S. O.; Govorov, A. O.; Gray, S. K.; Infante, I.; Sargent, E. H.; Scholes, G. D. Spectrally Resolved Ultrafast Exciton Transfer in Mixed Perovskite Quantum Wells. *J. Phys. Chem. Lett.* **2019**, *10* (3), 419–426.

(34)   Kikuchi, K.; Takeoka, Y.; Rikukawa, M.; Sanui, K. Structure and Optical Properties of Lead Iodide Based Two-Dimensional Perovskite Compounds Containing Fluorophenethylamines. *Curr. Appl. Phys.* **2004**, *4* (6), 599–602.

(35)   Mauck, C. M.; France-Lanord, A.; Hernandez Oendra, A. C.; Dahod, N. S.; Grossman, J. C.; Tisdale, W. A. Inorganic Cage Motion Dominates Excited-State Dynamics in 2D-

Layered Perovskites (C XH2x+1NH3)2PbI4 (x = 4-9). *J. Phys. Chem*. C **2019**, 123, 27904−27916

(36)   Akselrod, G. M.; Deotare, P. B.; Thompson, N. J.; Lee, J.; Tisdale, W. A.; Baldo, M. A.; Menon, V. M.; Bulovic, V. Visualization of Exciton Transport in Ordered and Disordered Molecular Solids. *Nat. Commun.* **2014**, *5*, 1–8.

(37)   Yang, S.; Niu, W.; Wang, A. L.; Fan, Z.; Chen, B.; Tan, C.; Lu, Q.; Zhang, H. Ultrathin Two-Dimensional Organic–Inorganic Hybrid Perovskite Nanosheets with Bright, Tunable Photoluminescence and High Stability. *Angew. Chemie - Int. Ed.* **2017**, *56* (15), 4252–4255.

(38)   Note that the ac and bc planes are indistinguishable in our measurements. For simplicity we refer to the ac plane for the remainder of this paper.

(39)   Li, J.; Ma, J.; Cheng, X.; Liu, Z.; Chen, Y.; Li, D. Anisotropy of Excitons in Two-Dimensional Perovskite Crystals. *ACS Nano* **2020**, *14* (2), 2156–2161.

(40)   Jurow, M. J.; Morgenstern, T.; Eisler, C.; Kang, J.; Penzo, E.; Do, M.; Engelmayer, M.; Osowiecki, W. T.; Bekenstein, Y.; Tassone, C.; Wang, L. W.; Alivisatos, A. P.; Brütting, W.; Liu, Y. Manipulating the Transition Dipole Moment of CsPbBr 3 Perovskite Nanocrystals for Superior Optical Properties. *Nano Lett.* **2019**, *19* (4), 2489–2496.

(41)   Schuller, J. A.; Karaveli, S.; Schiros, T.; He, K.; Yang, S.; Kymissis, I.; Shan, J.; Zia, R. Orientation of Luminescent Excitons in Layered Nanomaterials. *Nat. Nanotechnol.* **2013**, *8* (4), 271–276.

(42)   Mikhnenko, O. V.; Blom, P. W. M.; Nguyen, T. Q. Exciton Diffusion in Organic

         Semiconductors. *Energy Environ. Sci.* **2015**, *8* (7), 1867–1888.

(43)   Decrescent, R. A.; Venkatesan, N. R.; Dahlman, C. J.; Kennard, R. M.; Chabinyc, M. L.;

         Schuller, J. A. Optical Constants and Effective-Medium Origins of Large Optical

         Anisotropies in Layered Hybrid Organic/Inorganic Perovskites. *ACS Nano* **2019**, *13* (9),

         10745–10753.

(44)   Yin, J.; Maity, P.; Naphade, R.; Cheng, B.; He, J. H.; Bakr, O. M.; Brédas, J. L.;

         Mohammed, O. F. Tuning Hot Carrier Cooling Dynamics by Dielectric Confinement in

         Two-Dimensional Hybrid Perovskite Crystals. *ACS Nano* **2019**, *13* (11), 12621–12629.

(45)   Zhao, D.; Silva, R. E. F.; Climent, C.; Feist, J.; Fernández-Domínguez, A. I.; García-

         Vidal, F. J. Plasmonic Purcell Effect in Organic Molecules. arXiv:2005.05657, **2020**.

(46)   Baer, R.; Rabani, E. Theory of Resonance Energy Transfer Involving Nanocrystals: The

         Role of High Multipoles. *J. Chem. Phys.* **2008**, *128* (18), 184710.

(47)   Rowland, C. E.; Fedin, I.; Zhang, H.; Gray, S. K.; Govorov, A. O.; Talapin, D. V.;

         Schaller, R. D. Picosecond Energy Transfer and Multiexciton Transfer Outpaces Auger

         Recombination in Binary CdSe Nanoplatelet Solids. *Nat. Mater.* **2015**, *14* (5), 484–489.

(48)   Guzelturk, B.; Demir, H. V. Near-Field Energy Transfer Using Nanoemitters For

         Optoelectronics. *Adv. Funct. Mater.* **2016**, *26* (45), 8158–8177.

Supporting information

Efficient Interlayer Exciton Transport in Two-Dimensional Metal-Halide Perovskites.

Alvaro J. Magdaleno,[1,2] Michael Seitz,[1,2] Michel Frising,[1,2] Ana Herranz de la Cruz,[1,2] Antonio I. Fernández-Domínguez,[1,3] and Ferry Prins[1,2] *

1. Condensed Matter Physics Center (IFIMAC), Universidad Autonoma de Madrid, 28049 Madrid, Spain.

2. Department of Condensed Matter Physics, Universidad Autonoma de Madrid, 28049 Madrid, Spain.

3. Department of Theoretical Condensed Matter Physics, Universidad Autonoma de Madrid, 28049 Madrid, Spain.

AUTHOR INFORMATION

Corresponding Author

* Email: ferry.prins@uam.es

Sample preparation. Perovskite solutions were made following the recipes given in refs.[1–3] In short, n = 1 phenethylammonium lead iodine $(PEA)_2PbI_4$ solutions were prepared by mixing stoichiometric ratios of the precursor salts. Phenethylammonium iodide (PEAI) (Sigma Aldrich, 805904-25G) and lead(II) iodide (PbI_2) (Sigma Aldrich, 900168-5G) and were mixed with a stoichiometric ratio of 2:1 and dissolved in γ-butyrolactone (Sigma Aldrich, B103608-500G). The solution was heated to 70 °C while stirring until all the precursors were completely dissolved. The resulting solutions were kept at 70°C and the solvent was left to evaporate until reaching saturation of the solution. To obtain millimetre-sized single crystals, the saturated solutions were kept in a closed vial for about two weeks until the crystals appeared. Microscopy measurements on single crystals were performed by placing the crystal facet in contact with a cover slip using microscopy oil to avoid airgaps**.**

As an alternative to the large single crystals, smaller crystals (hundreds of micron lateral sizes) can be readily obtained using drop casting of the saturated perovskite solution on top of a microscope slide and heating to 50°C for 2-3 hours until drying. Interlayer measurements on the drop cast samples were performed by cleaving the microscope slide and subsequent sideways placement of the cleaved microscope slide onto a cover slip. As with the large single crystals, microscope oil was used to avoid air gaps. Crystallographic orientations of both samples were confirmed by measuring the polarization orientation of photoluminescent emission (see below). All diffusion measurements presented in this manuscript were performed on the large single crystal. It is important to note though, that no significant differences in the interlayer optical and transport characteristics were observed between of the large single crystals and the drop cast crystalline phases.

Absorbance and photoluminescence measurements. Absorbance spectra were obtained using a UV-Vis spectrophotometer (Mettler Toledo, UV7) on spin-coated layers of $(PEA)_2PbI_4$ (45 nm in thickness).[4] All photoluminescence measurements were performed with a sample mounted on an inverted microscope (Nikon TiU). To obtain photoluminescence spectra, samples were illuminated using a 385 nm light emitting diode (Thorlabs, M385LP1-C5). Emission spectra were recorded using an imaging spectrograph (Princeton Instruments, SpectraPro HRS-300, ProEM HS 1024BX3). Absorbance and emission spectra are consistent with literature reports for $(PEA)_2PbI_4$ and are shown in **Figure S1.**[5] For the polarization analysis the same set-up was used with the addition of a linear polarizer in the light path. The linear polarizer was rotated while acquiring the emission intensity for each polarizer orientation on a camera (Princeton Instruments, ProEM HS 1024BX3). Photoluminescence lifetime measurements were performed on the same inverted microscope, using pulsed 405 nm laser excitation (PicoQuant LDH-D-C-405, PDL 800-D, 10 MHz repetition rate). The photoluminescence was collected with an APD (Micro Photon Devices PDM, 20×20 μm detector size). The laser and APD were synchronized using a timing board for time correlated single photon counting (Pico-Harp 300). The resulting lifetime trace is shown in **Figure S2**.

Emission profile measurements. Perovskite crystals were excited with a 405 nm laser (PicoQuant LDH-D-C-405, PDL 800-D), which was focused down to a near diffraction limited spot. The laser spot images were acquired using an EMCCD camera coupled to a spectrograph (Princeton Instruments, SpectraPro HRS-300, ProEM HS 1024BX3) with a 150x magnification (NA 1.3, 100x oil immersion objective with an additional 1.5x tube lens magnification). Results are shown in **Figure 1D and S3**.

Exciton diffusion measurements. Exciton diffusion measurements were performed and analysed following the same procedure as previously reported by Seitz et al.[1]

Determination of optical constants. The $(PEA)_2PbI_4$ perovskite was modelled as a layered material composed of an alternating inorganic-organic layer stack. The effective medium model to calculate the intrinsic optical constants of the organic (PEA) and inorganic (PbI_4) layers follows the method described by DeCrescent et al.[6] The organic layer was considered isotropic, non-absorbing and to have a wavelength independent refractive index $n = 1.6$. The resulting constants for IP and OP components of the inorganic layer is depicted in **Figure S4**.
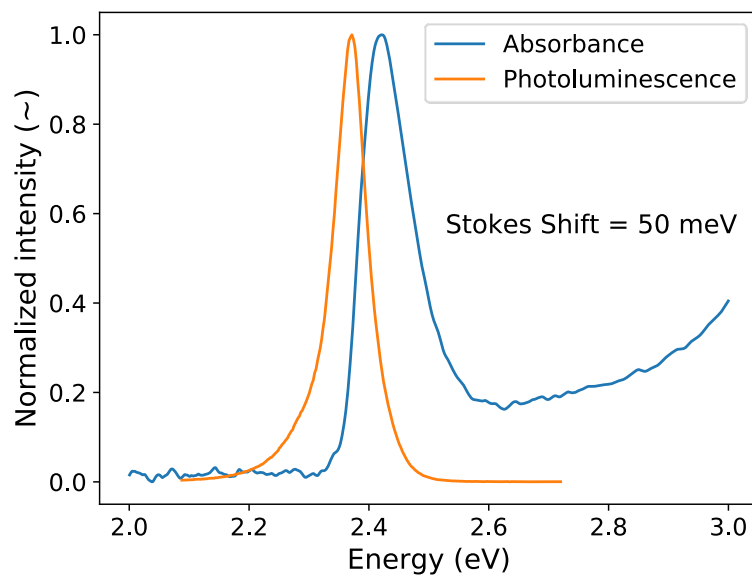

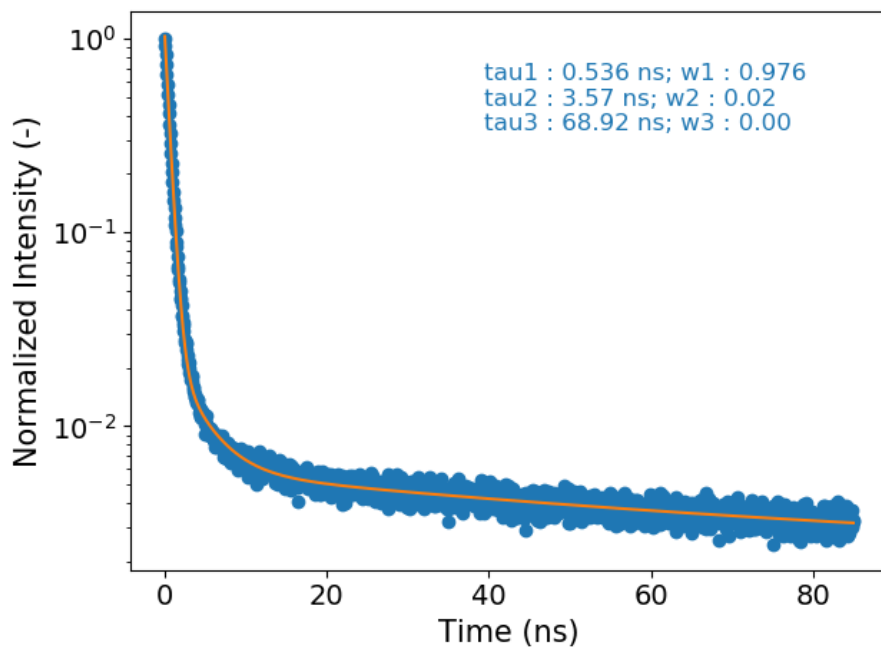**Figure S1.** Absorbance and photoluminescence spectra of $(PEA)_2PbI_4$ with a Stokes Shift of 50 meV.

Figure S2. Photoluminescence lifetime trace of $(PEA)_2PbI_4$ with a tri-exponential fit. Fitting parameters are given in the figure.

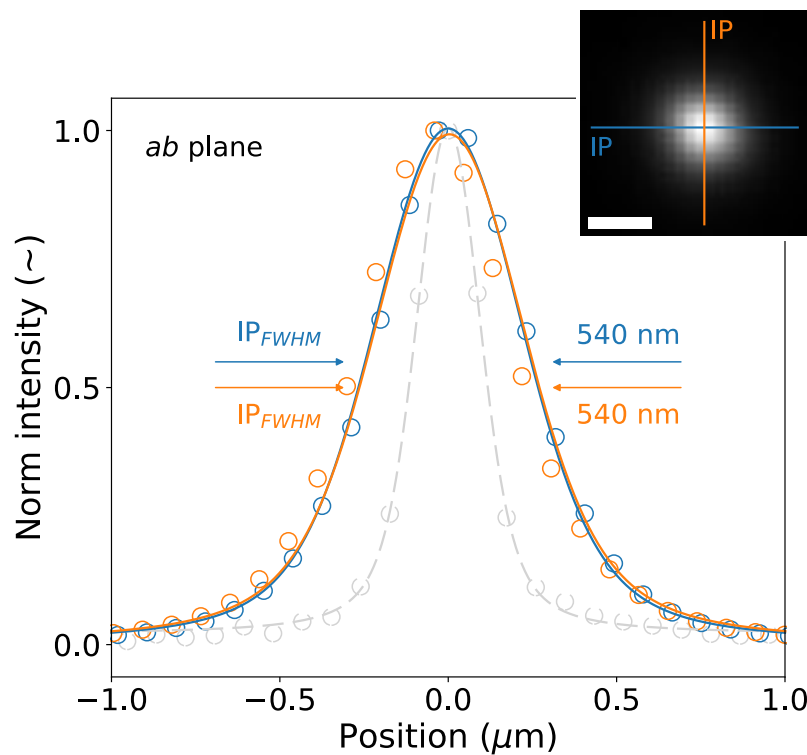**Figure S3.** Emission profile along the IP (blue and orange) axes from a near-diffraction limited excitation spot on the ab plane of a $(PEA)_2PbI_4$ crystal (see inset with a scale bar of 500 nm). Dashed grey line shows the laser excitation profile.

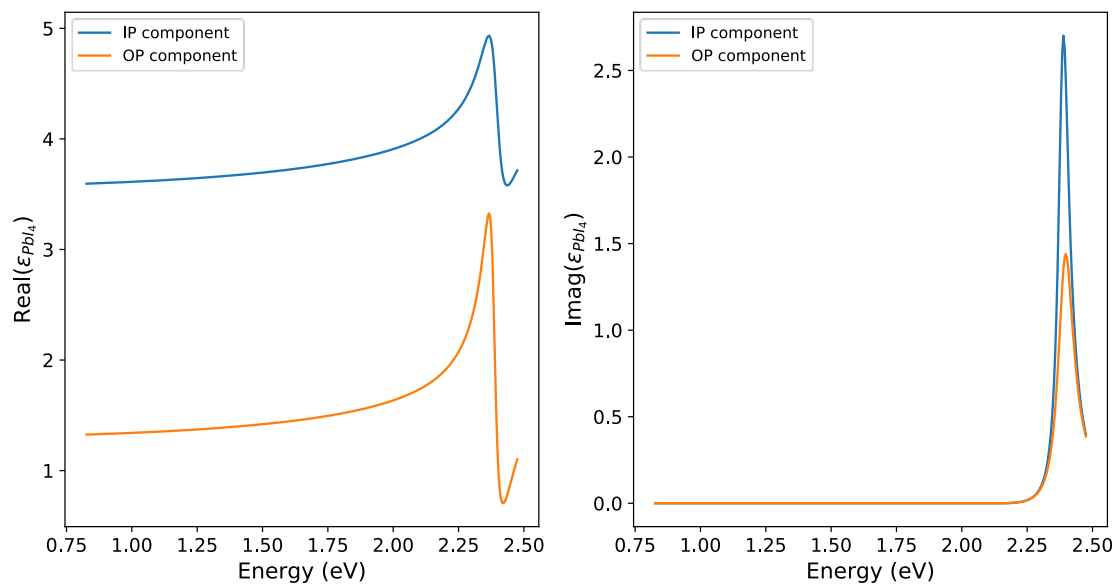**Figure S4.** Intrinsic dielectric function of the PbI$_4$ layer of the (PEA)$_2$PbI$_4$ perovskite calculated using an effective medium model.[6] The real and imaginary parts of the intrinsic dielectric function are shown on the left and right panels, respectively.

References

(1) Seitz, M.; Magdaleno, A. J.; Alcázar-Cano, N.; Meléndez, M.; Lubbers, T. J.; Walraven, S. W.; Pakdel, S.; Prada, E.; Delgado-Buscalioni, R.; Prins, F. Exciton Diffusion in Two-Dimensional Metal-Halide Perovskites. *Nat. Commun.* **2020**, *11* (1), 1–8.

(2) Seitz, M.; Gant, P.; Castellanos-Gomez, A.; Prins, F. Long-Term Stabilization of Two-Dimensional Perovskites by Encapsulation with Hexagonal Boron Nitride. *Nanomaterials* **2019**, *9* (8).

(3) Ha, S. T.; Shen, C.; Zhang, J.; Xiong, Q. Laser Cooling of Organic-Inorganic Lead Halide Perovskites. *Nat. Photonics* **2016**, *10* (2), 115–121.

(4) Zhang, S.; Audebert, P.; Wei, Y.; Choueiry, A. Al; Lanty, G.; Bréhier, A.; Galmiche, L.; Clavier, G.; Boissiére, C.; Lauret, J. S.; Deleporte, E. Preparations and Characterizations of Luminescent Two Dimensional Organic-Inorganic Perovskite Semiconductors. *Materials (Basel).* **2010**, *3* (5), 3385–3406.

(5) Kikuchi, K.; Takeoka, Y.; Rikukawa, M.; Sanui, K. Structure and Optical Properties of Lead Iodide Based Two-Dimensional Perovskite Compounds Containing Fluorophenethylamines. *Curr. Appl. Phys.* **2004**, *4* (6), 599–602.

(6) Decrescent, R. A.; Venkatesan, N. R.; Dahlman, C. J.; Kennard, R. M.; Chabinyc, M. L.; Schuller, J. A. Optical Constants and Effective-Medium Origins of Large Optical Anisotropies in Layered Hybrid Organic/Inorganic Perovskites. *ACS Nano* **2019**, *13* (9), 10745–10753.